Configuration-Dependent Electrically Tunable Van der Waals Heterostructures Based on $MoTe_2/MoS_2$

*Feng Wang, Lei Yin, Zhen Xing Wang, Kai Xu, Feng Mei Wang, Tofik Ahmed Shifa, Yun Huang, Chao Jiang, and Jun He**

Van der Waals heterostructures (vdWHs), obtained by artificially stacking 2D layered material (2DLM) plains upon each other, are brand new structures that have exhibited novel electronic and optoelectronic properties and attracted a great deal of attention. So far, the results are only based on devices with symmetrical configurations: devices predominated by vdWH parts, or cross-like configurations combined with both vdWHs and extra individual 2DLM layers. Quite different gate tunable phenomena have been observed for these two configurations even though 2DLMs with similar band alignments were used, which may be due to the different device configurations utilized. For a deeper understanding, rational investigation on configuration-dependent properties of vdWHs is needed. Here, using $MoTe_2/MoS_2$ as an example, vdWH device is artificially designed with two asymmetrical configurations. Through comparing the respective results, it is found that the properties that stem only from the vdWH, i.e., the rectification behavior and open voltage in photovoltaic effect, are independent of the device structures. However, other properties, i.e., drain currents, short circuit currents, and photoreponse performances, strongly depend on the configuration used. These results give a guideline on studying the intrinsic properties of vdWHs and optimizing the device structures for better performances.

1. Introduction

By artificially stacking isolated planes of different 2D layered materials (2DLMs) on top of each other, one can obtain heterostructures with thickness of only a few nanometers.[1–4] Due to the dangling bonds free surfaces of 2DLMs, the as fabricated heterostructures are vertically kept together by van der Waals forces between adjacent planes.[3] Hence they are also known as van der Waals heterostructures (vdWHs).[1] Theoretically, vdWHs can be made up with any 2DLM planes in any sequences, which greatly enriches the choices of materials with desired properties.[1,5,6] Specially, through assembling p- and n-type 2DLMs together, we can fabricate atomically sharp van der Waals p–n junctions.[7] As the most essential building blocks of logic circuits, light emitting diodes (LEDs) and solar cells, etc., p–n junctions are the fundamental of modern electronic technology. Considering the impossibility of using traditional method to dope the ultrathin bodies of 2DLMs, vdWH is one of the best ways to achieve p–n junctions in this scenario. In addition, taking advantages of the novel properties of individual 2DLMs (a) high carrier mobility because of the absent surface scattering from dangling bonds,[8,9] (b) wide coverage of band gaps (≈0.3–6 eV),[10,11] and (c) high compatibility with traditional devices fabrication process as well as flexible substrates resulting from their 2D geometry, vdW p–n junctions exhibit promising potentials for next generation of electronic and optoelectronic devices.[2] What is more, vdW p–n junctions usually show strong light-matter interaction as the fact that most 2DLMs can form type II band alignment and their 2D configuration endows them ultrahigh specific surface areas.[6,11–13] Taking MoS_2/WS_2 heterostructure as an example, it takes only 50 fs for photo-stimulated holes to transfer from the valence band of MoS_2 to the WS_2 layer.[14] Inspired by these advantages, a number of vdW p–n junctions, such as WSe_2/MoS_2,[7,15,16] black phosphorus/MoS_2,[17] WS_2/MoS_2,[18] GaTe/MoS_2,[19] and $MoTe_2/MoS_2$[20] have been fabricated and demonstrated with extraordinary performances. For instance, using GaTe and MoS_2 as holes and electrons providers, our group recently fabricated GaTe/MoS_2 vdW p–n junctions which exhibited rectification ratio (RF), external quantum efficiency, and selective detectivity of as high as 4×10^5, 61.68%, and 8.4×10^{13} Jones, respectively.[19] Moreover, due to their ultrathin thickness and steep interfacial charge carrier gradient, 2D vdW p–n junctions show strong electrical tunability on electronic and optoelectronic properties, which offers a way to achieve the functional ends and, more importantly, to understand the underlying working mechanisms.[7,21,22]

In addition to the advantages displayed on electronic and optoelectronic devices, vdW p–n junctions also show novel phenomena due to their ultrathin thickness. For example, unlike the built-in potential and space charge region in conventional p–n junctions, it was found that the tunneling-assisted interlayer recombination of the majority carriers may be responsible for the electrically tunable rectification and PV effects observed in atomically thin WSe_2/MoS_2 p–n junction.[7,16] Being a newly emerged research field, even though many works have already

F. Wang, L. Yin, Prof. Z. X. Wang, K. Xu, F. M. Wang, T. A. Shifa, Y. Huang, Prof. C. Jiang, Prof. J. He
CAS Key Laboratory of Nanosystem and Hierarchical Fabrication
National Center for Nanoscience and Technology
Beijing 100190, P.R. China
E-mail: hej@nanoctr.cn

DOI: 10.1002/adfm.201601349

© 2016 WILEY-VCH Verlag GmbH & Co. KGaA, Weinheim

been done, the fundamental mechanism of vdW p–n junctions is still unclear and the top limit of their performances is also remained unexplored hitherto. So far, two kinds of artificially stacked symmetry device structures have been used to study the vdW p–n junctions, both of which displayed strong electrically tunable electronic and optoelectronic properties. The first one is cross-like device structure, in which the whole device is a series connection of overlapping part (vdW p–n junction) and extra individual 2DLMs parts.[7,19,21] However, due to the strong gate tunability of individual 2DLMs parts as well, the observed phenomena were probably not only from the vdW p–n junctions but a superposition of these two parts, which have been ignored by the authors. On the other hand, devices predominated by vdW p–n junction parts were also fabricated. Notably, compared with the cross-like device structure, quite different gate tunable properties were observed, both in WSe_2/MoS_2 and black phosphorus/MoS_2, although materials with similar band alignment were used.[16,17] One reason for this inconsistence may be due to the different device structures used. For a deeper understanding of vdW p–n junctions, rational investigation on device structure-dependent properties of vdW p–n junctions is needed.

Here we report configuration-dependent electrically tunable $MoTe_2/MoS_2$ vdWHs. The vdWHs show gate voltage tunable rectification characteristics, photovoltaic (PV) effects, and photoresponse properties. More importantly, by designing the devices with two asymmetry structures at the same time, we found that the rectification behavior and open voltage are independent of the configuration used. However, the drain currents, short circuit currents, and photoreponse performances strongly depend on the device structures. Higher PV effects, photoresponsivity, and faster photoresponse times were observed in the device that vdWH part predominate the structure. On the other hand, device with extra individual part exhibits higher selective photodetctivity. These results provide a guideline on studying the intrinsic properties of vdWHs and optimizing the device structures for better desired performances.

2. Results and Discussion

2.1. Device Characterization

All the devices used in the experiments were fabricated by mechanical exfoliation combined with directional transfer method (see the Experimental Section for detail).[19,23] To study the effect of configuration on the device performances, we artificially designed an asymmetric device structure. **Figure 1**a,d shows the schematic diagram and the optical microscope image of the final device, respectively. Due to the asymmetric device structure, two different circuit models (Figure 1b,c) will be induced while using different source/drain electrodes (E1–E4 shown in Figure 1d). To be specific, MoS_2 is one of the most studied n-type 2DLMs.[8] On the other hand, $MoTe_2$ is a recently discovered ambipolar 2DLMs with distinctive properties.[24,25] As shown in the inset of Figure 1a, the two 2DLMs share a

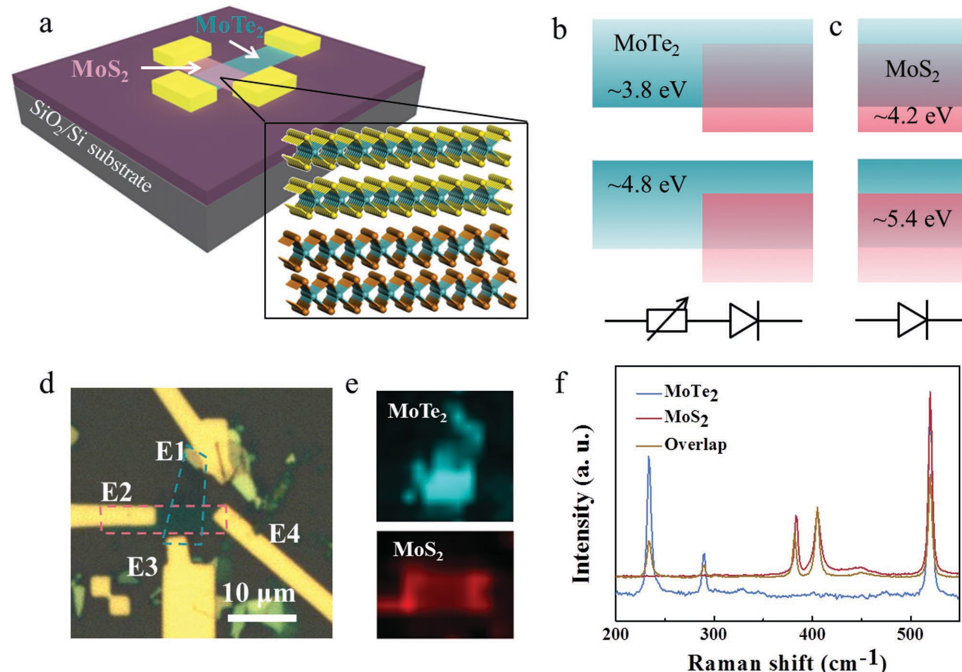

Figure 1. a) Schematic diagram of the $MoTe_2$ (cyan)/MoS_2 (pink) vdWH device. Few-layer MoS_2 was exfoliated on the top of the $MoTe_2$ flake, and 8/60 nm Cr/Au was used as electrode. The inset shows the enlarged crystalline structures of $MoTe_2$ and MoS_2, with cyan, yellow, and brown balls representing Mo, S, and Te atoms, respectively. Band diagrams of devices while using b) E1/E2 and c) E3/E4 as source/drain electrode pairs. A type II band alignment formed at the overlapping region. The corresponding equivalent circuit diagrams are shown at the bottom. d) Optical microscope image of the device, where E1–E4 show the four electrodes. e) Spatially resolved Raman maps for the $MoTe_2$ (top panel, Raman shift at 234 cm^{-1}) and the MoS_2 flakes (bottom panel, Raman shift at 384 cm^{-1}). f) Raman spectra collected from the different positions of the device: the blue, red, and brown lines come from the $MoTe_2$, MoS_2, and the overlapping region respectively.

© 2016 WILEY-VCH Verlag GmbH & Co. KGaA, Weinheim
Adv. Funct. Mater. 2016, DOI: 10.1002/adfm.201601349

similar crystal structure: hexagonally packed planes of Mo atoms sandwiched with two planes of chalcogen (S or Te) atoms. Due to the band positions of the two materials, a vdWH with a type II band alignment would form at the overlapping region, as shown in Figure 1b,c.[13,26] For the case where E3 and E4 were used as source/drain electrode pair, the vdWH would dominate the device performances. On the contrary, if E1 and E2 were used, the extra $MoTe_2$ part would act as an adjustable resistor and may affect the overall device performances. Note that there are also two tiny parts of extra MoS_2 for using E1/E2 as well as E3/E4 electrode pairs. However, considering the comparable and relatively small sizes of these two parts (6–7 times smaller than the overlapped part and the extra $MoTe_2$ part), we ignored their influences, which we believe would not affect the final results that based on comparative study of E1/E2 and E3/E4. Figure 1b,c depicts the respective band diagrams and equivalent circuit models (see the following discussions). In addition, according to our recent works on $MoTe_2$ and MoS_2, we chose Cr as the direct contact metal, having a matched work function with both of these two materials which enables it to reduce the Schottky barriers at the semiconductor/electrode interfaces and highlight the role of the channels.[19,27] The thicknesses of the $MoTe_2$ and MoS_2 flakes are around 1.5 (about two layers) and 3.8 nm (about 10 layers), respectively, as defined by atomic force microscope (AFM, see Figure S1, Supporting Information). Raman spectroscopy was used to confirm the quality of the vdWH. The Raman maps (Figure 1e) further illustrates the structure of our device. Obvious changes in the intensity of the peaks were observed at the overlapping region, which probably emanates from the interaction between the two flakes.[19] The Raman spectrum of the overlapping part (brown line in Figure 1f) is a combination of bottom $MoTe_2$ (blue line in Figure 1f, at Raman shifts of about 234 and 298 cm^{-1})[28] and top MoS_2 (red dot dot line in Figure 1f, at Raman shifts of about 384 and 405 cm^{-1}),[29] demonstrating the formation of the vdWH.

2.2. Configuration-Dependent Electronic Properties of the $MoTe_2/MoS_2$ vdWHs

Next, the electronic properties of the device were studied by using different electrode pairs (E1/E2 and E3/E4). The whole measurements were taken in vacuum (about 10^{-5} Torr) to eliminate the effect of atmosphere. And we considered $MoTe_2$ as anode for the electronic measurements. **Figure 2**a shows the transfer curves of the individual flakes. The MoS_2 and $MoTe_2$ exhibit distinct n-type and ambipolar behaviors (p-type dominates), respectively, agreeing well with the former reports.[8,24] Figure 2b shows the transfer curves while using different electrode pairs that are distinctly different from the individual ones. Specifically, the drain currents (I_{ds}) show a peak at about gate voltage (V_g) = −40 V, and a tail at $V_g > 0$ V when E3/E4 or E3/E2 was used. This can be understood by taking the device structure as well as the individual transfer curves into consideration. From Figure 1d we can see that the overlapping regions (vdWH) dominate the device at this condition. For the $MoTe_2/MoS_2$ vdWH, which can be treated as a series connection of $MoTe_2$ and MoS_2 channels, the I_{ds}–V_g curve can be divided into the following three parts: (a) $V_g < \approx -40$ V and $\approx 0 \text{ V} > V_g > \approx -40$ V. In these regions, I_{ds} decreases due to the increasing resistance of either MoS_2 (for $V_g < \approx -40$ V) or $MoTe_2$ flake (for $V_g > \approx -40$ V), (b) $V_g \approx -40$ V. At this V_g, I_{ds} reaches a maximum value owing to the moderate non-zero conductance of both MoS_2 and $MoTe_2$, (c) $V_g > \approx 0$ V. Here, I_{ds} increases as a result of the increasing conductance of MoS_2 that dominates over the total performances of the device. The corresponding dominated device components for different ranges of V_g are indicated by different colors as seen in Figure 2b. However, the tail at $V_g > 0$ V disappears when E1/E2 or E1/E4 is employed. This is because, in this case, the device is not just the overlapping region but a series connection of $MoTe_2/MoS_2$ vdWH and a gate-tunable resistance (extra $MoTe_2$). Figure 1b depicts the equivalent circuit model. The resistance of the extra $MoTe_2$ part increases when V_g increases. Consequently, the I_{ds} at $V_g > 0$ V are smaller than the peak value at this condition. To confirm our speculation, two other devices but with relatively larger MoS_2 part (Figure S2a, Supporting Information) or much more $MoTe_2$ part (Figure S2c, Supporting Information) were fabricated. For the former, as shown in Figure S2b in the Supporting Information, the transfer curve shows a sharply downward trend at $V_g < 0$ V due to the off state of MoS_2 at this V_g range. On the other hand, the latter device (Figure S2d, Supporting Information) exhibits an exactly similar trend with individual $MoTe_2$, conveying the fact that the electronic performances are dominated by $MoTe_2$ due to the special device structure. Note the enhanced ambipolar behavior and improved drain current may probably come from the thicker thickness.[30] In addition, the gate voltage dependent resistances of divided parts for the two structures are quantitatively analyzed and shown in Figure S3 in the Supporting Information, which further demonstrates the differences between using E1/E2 and E3/E4 electrode pairs.

We then studied the configuration-dependent rectification behaviors of our device. Figure 2c,e shows the current-bias voltage (I_{ds}–V_{ds}) curves in logarithmic scale under different gate voltages while using E1/E2 and E3/E4 as source/drain electrodes, respectively (the curves in linear scale are given in Figure S4a,b, Supporting Information). The corresponding gate voltages dependent drain current values at $V_{ds} = 2/-2$ V ($I_{forward}$ and $I_{reverse}$) were extracted and are shown in Figure 2d and f, respectively. Parallel with the transfer curves shown in Figure 2b, the $I_{forward}$ and $I_{reverse}$–V_g relationships exhibit a similar but more obvious difference while using different electrode pairs: the $I_{forward}$ and $I_{reverse}$ show peaks at $V_g \approx -40$ V when E1/E2 was used, on the other hand, $I_{forward}$ and $I_{reverse}$ show peaks as well as tails when E3/E4 is used. However, the RF (defined as RF = $|I_{forweard}/I_{reverse}|$) show an exactly similar trend for these two conditions. This is because the rectification behavior wholly depends on the vdWH part, which is quite the same for the two cases. Together, the above analysis demonstrates that the electronic properties stemming from vdWH is independent of the configuration used, however, the others strongly rely on the device structure.

2.3. Configuration-Dependent Photovoltaic Effects of the $MoTe_2/MoS_2$ vdWHs

Based on the electronic properties shown above, we further studied the configuration-dependent PV effects of the device.

© 2016 WILEY-VCH Verlag GmbH & Co. KGaA, Weinheim

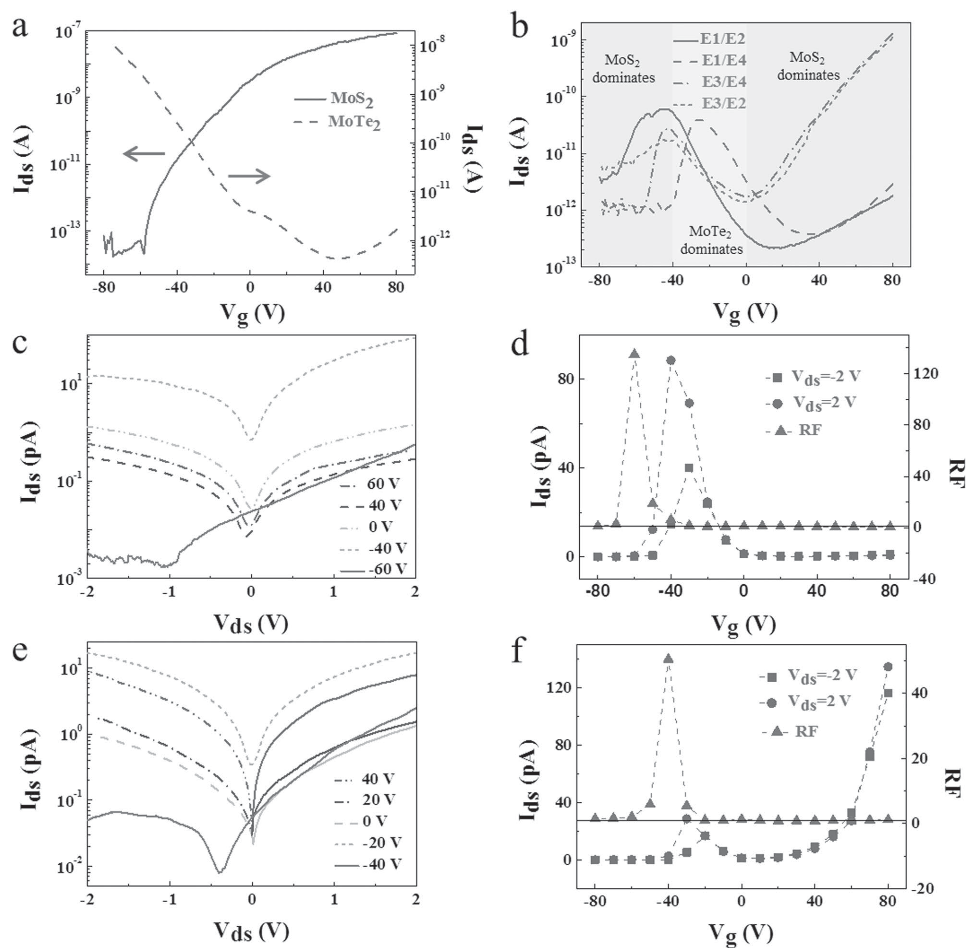

Figure 2. a) Transfer curves of the individual $MoTe_2$ (dash line) and MoS_2 (solid line) flakes. V_{ds} = 2 and 0.5 V, respectively. b) Transfer curves of the device while using E1/E2 (solid line), E1/E4 (dash line), E3/E4 (dash dot line), and E3/E2 (short dash line) were used as electrode pairs, respectively. V_{ds} were set at 2 V for the above measurements. The dominated roles for different gate voltage ranges are indicated by different colors. The drain current-bias voltage characteristics in logarithmic scale at different gate voltages were shown in (c) using E1/E2 electrode pairs and (e) using E3/E4 electrode pairs, respectively. The corresponding drain currents at V_{ds} = 2 V (circles), −2 V (squares) as well as RF (triangles) were extracted and shown in (d) and (f), respectively. The black lines indicate the RF values of 1.

For the whole measurement, a 473 nm laser with a power density of 65 mW cm^{-2} was used as the light source. Considering the band gap values of $MoTe_2$ (≈1.0 eV) and MoS_2 (≈1.2 eV), both of them are expected to response to the incident light, which have been demonstrated by the previous works.[27,31] **Figure 3**a,c shows the gate voltage tunable I_{ds}–V_{ds} curves under illumination when E1/E2 and E3/E4 were used, respectively. As we can see that all the curves pass through the fourth quadrant while under illumination, confirming the presence of PV effects for both device structures. The corresponding relationships between open circuit voltages (V_{oc})/short circuit currents (I_{sc}) and gate voltages were extracted and are shown in Figure 3b and d, respectively. For both structures, V_{oc} increases with scanning of V_g from −80 to 60 V and then decreases with that of V_g from 60 to 80 V (up to 0.17 and 0.16 V, respectively). This trend can be explained by the gate tunable band diagrams shown in Figure 3e. $MoTe_2$ exhibit p-type conduction (see Figure 2a) while 60 V > V_g > −80 V, suggestive of the phenomena that the overlapping part forms a vdW p–n junction. According to the conventional p–n junction theory, qV_{oc} is proportional to $|E_{Fp}–E_{Fn}|$, where q, E_{Fp}, and E_{Fn} are the elementary charge, Fermi levels of p-type and n-type semiconductors, respectively.[32] For our device, $MoTe_2$ exhibit stronger gate tunability due to its bottom position as well as its ambipolar behavior.[17,19] As a consequence, the difference of Fermi levels between $MoTe_2$ and MoS_2 increased gradually while scanning V_g from −80 to 60 V as depicted in the left and middle panels of Figure 3e. Hence, the V_{oc} increase in this V_g range. However, $MoTe_2$ exhibit n-type conduction for V_g > 60 V (Figure 2a), leading to an n–n junction at the overlapping region, hence a decreasing trend of V_{oc} was induced (right panel of Figure 3e).[16] It is notable that the V_{oc} experience the same trend for these two structures, signifying the fact that the PV effect only comes from the vdWH part and is largely independent with the configuration used. This evidently corroborates the RF–V_g relationships discussed above. We note that there are tiny differences in V_{oc} between the two structures, which may come from the different carrier transport paths, unintentional doping from the substrate and measurement accuracy.[32,33] While illuminated, the device can be treated as a

© 2016 WILEY-VCH Verlag GmbH & Co. KGaA, Weinheim

DOI: 10.1002/adfm.201601349

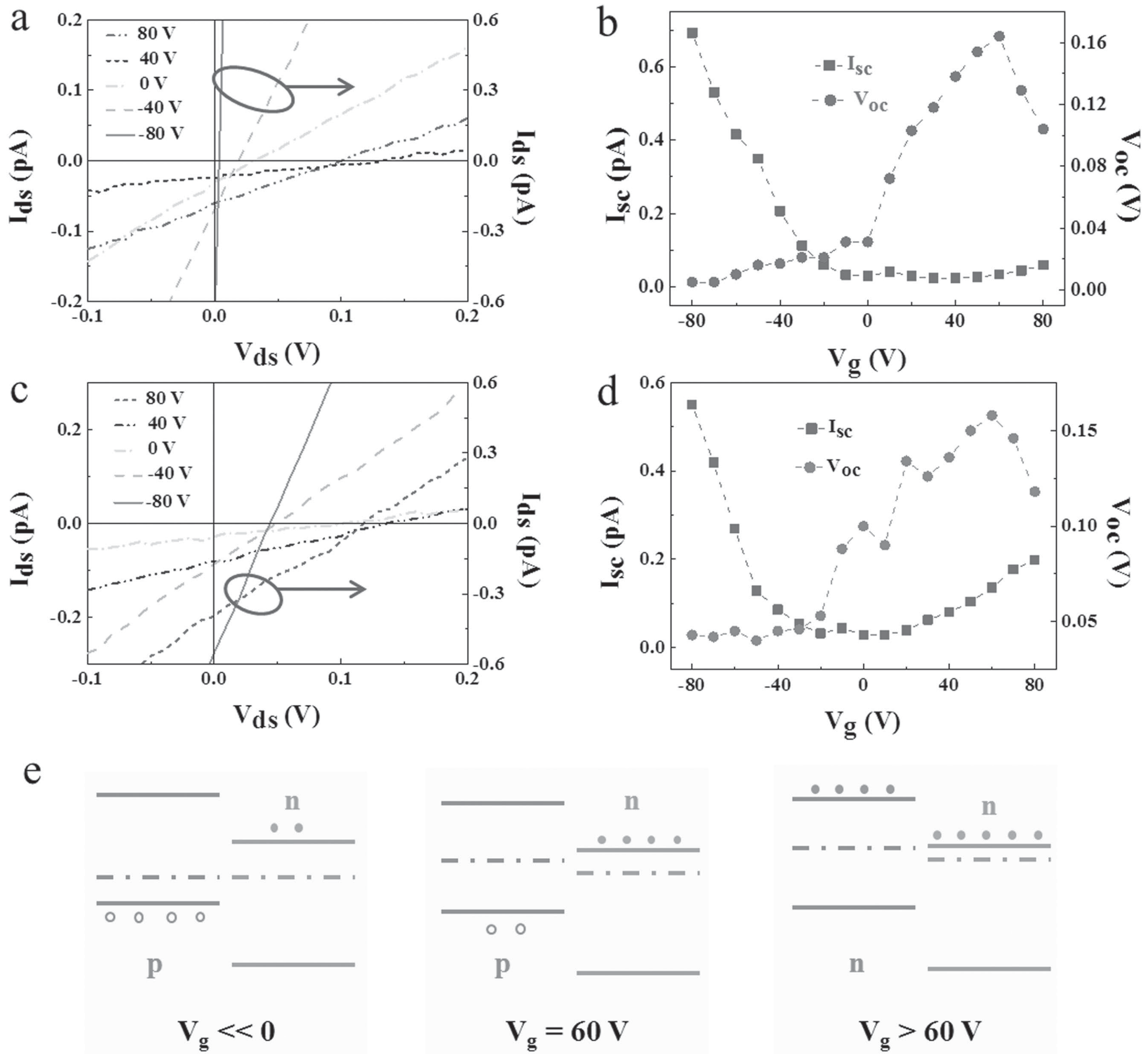

Figure 3. The enlarged partial drain current-bias voltage characteristics at different gate voltages (80, 40, 0, −40 and −80 V) while under illumination were shown in (a) using E1/E2 and (c) using E3/E4 electrode pairs, respectively. b,d) The extracted short circuit currents (squares) and open circuit voltages (circles). e) Band alignment profiles of the $MoTe_2/MoS_2$ vdWHs at gate voltages ≪ 0 V (left panel), = 60 V (middle panel) and >60 V (right panel). The solid and open circles stand the electrons of holes, respectively. For the measurement, a 473 nm laser with a diameter of 5 mm was used as light source.

power source series connected with a gate adjustable load. As a result, when E3/E4 are used as source/drain pair, I_{sc} increases gradually for $V_g > 0$ V because of the increasing power supply (V_{oc}) as well as the decreasing load (Figure 2f, the above analysis). On the contrary, although V_{oc} increased, I_{sc} was basically flat due to the increasing load (Figure 2d) while using E1/E2. Similar relationships of V_{oc}/I_{sc}–V_g have been also observed in another device (see Figure S5a,b, Supporting Information), demonstrating the representativeness of the PV effects shown here. Electrical power (P_{el}), defined as $P_{el} = I_{ph}V_{ph}$, and filling factor (FF), defined as $FF = P_{el,max}/I_{sc}V_{oc}$, where I_{ph}, V_{ph}, and $P_{el,\,max}$ are photocurrent, photovoltage, and the maximum electrical power, respectively, are also two other figures of merit to evaluate PV effect.[16,19] The $P_{el,\,max}$–V_g and FF–V_g relationships were calculated and the result is shown in Figure S4c,d, respectively in the Supporting Information. Both of these two merits demonstrate a better performance while using E3/E4 (an average FF of 0.27 for E3/E4 compared with 0.25 for E1/E2), which is probably because of the extra load of E1/E2 structure.

2.4. Configuration-Dependent Photoresponse of the $MoTe_2/MoS_2$ vdWHs

The configuration-dependent photoresponse properties of the device were also studied. **Figure 4**a,b shows the corresponding

© 2016 WILEY-VCH Verlag GmbH & Co. KGaA, Weinheim

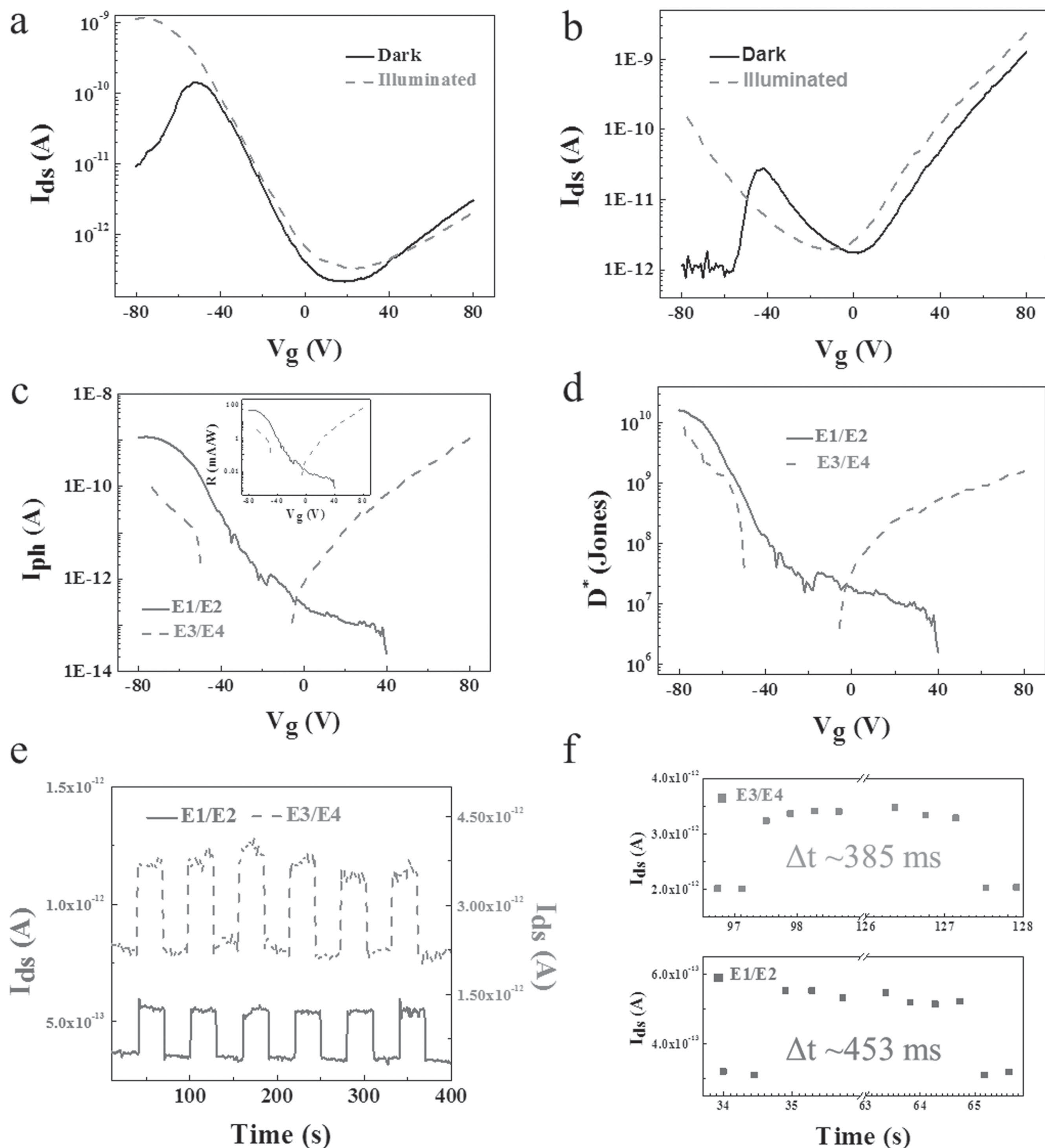

Figure 4. The transfer curves under dark (solid lines) and illuminated (dash lines) states while using a) E1/E2 and b) E3/E4 electrode pairs. V_{ds} were set as 2 V. c) Gate voltage dependent photocurrents for devices using E1/E2 (solid line) and E3/E4 (dash line) electrode pairs. The inset shows the corresponding gate voltage dependent photoresponsivities of the two device structures. d) Gate voltage dependent selective detectivity for devices using E1/E2 (solid line) and E3/E4 (dash line) electrode pairs. e) The time-dependent drain currents under periodic illumination for devices using E1/E2 (solid line) and E3/E4 (dash line) electrode pairs, respectively. f) Time resolved photoresponse characteristics for devices using E1/E2 (squares) and E3/E4 (squares) electrode pairs. The respective response times were extracted and shown in the figure. V_{ds} = 2 V. And a 473 nm laser with a diameter of 5 mm was used as light source.

transfer curves under dark and illuminated states while using E1/E2 and E3/E4 electrodes, respectively. Like the individual transfer curves under dark state, the curves in the illuminated case show similarly ambipolar behavior but with distinctive difference between two structures. The negative photoresponse phenomena while V_g > 40 V for E1/E2 structure and –6 V > V_g > –50 V for

© 2016 WILEY-VCH Verlag GmbH & Co. KGaA, Weinheim
Adv. Funct. Mater. **2016**,
DOI: 10.1002/adfm.201601349

E3/E4 structure may come from the photogating effect.[27,34,35] For convenience, we hereby only discuss the positive photoresponse parts. Figure 4c shows the photocurrent (I_{ph})–V_g relationships of two device structures. Compared with E1/E2, the I_{ph} show an 'ambipolar' behavior for E3/E4 due to the on states of the both ends of V_g. Note that a 473 nm (corresponds to phonon energy of about 2.8 eV) laser was used as light source, which can generate the photo-stimulated electron–hole pairs both in $MoTe_2$ (with $E_g \approx 1$ eV) and MoS_2 (with $E_g = \approx 1.2$ eV). Hence a comparable maximum I_{ph} ($\approx 1.1 \times 10^{-9}$ A) was detected for both device structures. The corresponding V_g-dependent photoresponsivities (R), defined as $R = I_{ph}/P_{ph}$, where P_{ph} is the incident light power, were calculated and given in the inset of Figure 4d.[34,36] Alike with I_{ph}, R–V_g relationships show a similar difference between these two structures: a maximum R of 47 mA W^{-1} was achieved at $V_g = -76$ V for E1/E2, however the highest R of 64 mA W^{-1} was achieved at $V_g = 80$ V for E3/E4. The comparable peak I_{ph} and different R values indicate that the vdWH part obtain a higher photoelectric conversion efficiency. Specific detectivity (D^*), defined as $D^* = (A\Delta f)^{1/2}/\text{NEP}$, where A is the effective detecting area in cm^2, Δf is the electrical bandwidth in Hz, and NEP is the noise equivalent power, is another important parameter to evaluate the photoresponse performances.[37,38] By assuming that dark current is the major contributor to shot noise, D^* can be expressed as $I_{ph}A^{1/2}/PA(2qI_{dark})^{1/2}$.[38] The calculated corresponding D^* are shown in Figure 4d. Unlike the I_{ph} and R, E1/E2 structure shows a higher maximum D^* of 1.6×10^{10} Jones, which is due to the lower dark current compared with E3/E4 structure. Figure 4e shows the time dependence of I_{ds} under periodic illumination for the two device structures. Both of them display a good stability of photoresponse with photo switching on/off ratio of ≈2. The time-resolved photoresponse performances were also studied. As shown in Figure 4f, a faster response time (defining as the time differences between the off-/on-state currents) of ≈385 ms was detected for E3/E4 structure, which is probably due to the higher dissociation efficiency of vdWHs as well as shorter transport path of E3/E4 compared with E1/E2 structure. The relatively slow response speed is probably attributed to the charge trap defects at the material/substrate and material/electrode interfaces during device fabrication. In addition, the good stability of photoresponse and response speed were also observed in another independent device, as shown in Figure S5c,d in the Supporting Information, which demonstrates the representativeness of the photoresponse performances shown here.

3. Conclusion

In summary, using $MoTe_2/MoS_2$ as a sample, the configuration-dependent electrically tunable electronic and optoelectronic properties of vdWHs were studied. Through comparing the properties from two different vdWH device structures, we found that the properties that only emanate from the vdWHs, i.e., the rectification behavior and open voltage of PV effect, are independent of the device structures. However, other property, i.e., drain currents, short circuit currents, and photoreponse performances, strongly depend on the type of structures employed. The device dominated by vdWH part exhibits higher PV effects, photoresponsivity, and faster photoresponse times. On the other hand, device with extra individual part exhibits higher selective photodetectivity. These results give a guideline on studying the intrinsic properties of vdWHs as well as optimizing the device structures.

4. Experimental Section

Device Fabrication: The devices were fabricated by mechanical exfoliation and a targeted transfer method. Firstly, few-layer $MoTe_2$ was exfoliated by standard scotch method from the bulk crystal (99.995%, HQ Graphene) onto 300 nm SiO_2/Si wafers, which had been cleaned with a piranha solution for 2 h. The thickness of the $MoTe_2$ was verified by OM and AFM. Then, PVA and PMMA were sequentially spin-coated on the top of another SiO_2/Si substrate. After that, MoS_2 (purchased from SPI) was then exfoliated onto the SiO_2/PVA/PMMA substrate. After dissolving the PVA layer in DI-water, the PMMA film carrying exfoliated MoS_2 was floated and then mounted on the arm of a micromanipulator. MoS_2 was then transferred directionally to the target $MoTe_2$ flake. During the transfer, the target wafer was heated to 180 °C to ensure a good adhesion between the PMMA and the bottom wafer. The PMMA was removed by acetone. Finally, the heterostructure was annealed in hydrogen/argon environment (H_2:Ar = 5:95) at 200 °C for 2 h to eliminate any possible contamination at the $MoTe_2/MoS_2$ interface. Electrode patterns were defined by standard EBL, and 8/60 nm Cr/Au electrodes were deposited by thermal evaporation.

Device Characterization: The morphology, material quality, and thickness characterizations were performed by OM (Olympus BX51 M), Raman spectroscopy (Renishaw InVia, 532 nm excitation laser), and AFM (Veeco Multimode), respectively. The electrical transport measurements were carried out on a probe station (Lakeshore, TTP4) equipped with a vacuum pump and a semiconductor characterization system (Keithley 4200). The optoelectronic properties were measured using a 473 nm laser with a diameter of 5 mm and maximum light intensity of 12.77 mW (RGBLase).

Supporting Information

Supporting Information is available from the Wiley Online Library or from the author.

Acknowledgements

This work was supported by the National Natural Science Foundation of China (Nos. 21373065, 61474033, and 61574050), Strategic Priority Research Program of the Chinese Academy of Sciences (Grant No. XDA09040201), 973 Program of the Ministry of Science and Technology of China (No. 2012CB934103), and CAS Key Laboratory of Nanosystem and Hierarchical Fabrication. The authors also gratefully acknowledge the support of Youth Innovation Promotion Association CAS.

Received: March 16, 2016
Revised: May 9, 2016
Published online:

[1] A. K. Geim, I. V. Grigorieva, *Nature* **2013**, *499*, 419.
[2] a) W. J. Yu, Z. Li, H. L. Zhou, Y. Chen, Y. Wang, Y. Huang, X. F. Duan, *Nat. Mater.* **2013**, *12*, 246; b) L. Britnell, R. V. Gorbachev, R. Jalil, B. D. Belle, F. Schedin, A. Mishchenko, T. Georgiou, M. I. Katsnelson, L. Eaves, S. V. Morozov, N. M. R. Peres, J. Leist, A. K. Geim, K. S. Novoselov, L. A. Ponomarenko, *Science* **2012**,

© 2016 WILEY-VCH Verlag GmbH & Co. KGaA, Weinheim

335, 947; c) W. J. Yu, Y. Liu, H. L. Zhou, A. X. Yin, Z. Li, Y. Huang, X. F. Duan, *Nat. Nanotechnol.* **2013**, *8*, 952.

[3] a) H. Wang, F. C. Liu, W. Fu, Z. Y. Fang, W. Zhou, Z. Liu, *Nanoscale* **2014**, *6*, 12250; b) F. Wang, Z. X. Wang, Q. S. Wang, F. M. Wang, L. Yin, K. Xu, Y. Huang, J. He, *Nanotechnology* **2015**, *26*, 292001.

[4] Y. Cao, A. Mishchenko, G. L. Yu, E. Khestanova, A. P. Rooney, E. Prestat, A. V. Kretinin, P. Blake, M. B. Shalom, C. Woods, J. Chapman, G. Balakrishnan, I. V. Grigorieva, K. S. Novoselov, B. A. Piot, M. Potemski, K. Watanabe, T. Taniguchi, S. J. Haigh, A. K. Geim, R. V. Gorbachev, *Nano. Lett.* **2015**, *15*, 4914.

[5] T. Roy, M. Tosun, J. S. Kang, A. B. Sachid, S. B. Desai, M. Hettick, C. M. C. Hu, A. Javey, *ACS Nano* **2014**, *8*, 6259.

[6] F. Withers, O. Del Pozo-Zamudio, A. Mishchenko, A. P. Rooney, A. Gholinia, K. Watanabe, T. Taniguchi, S. J. Haigh, A. K. Geim, A. I. Tartakovskii, K. S. Novoselov, *Nat. Mater.* **2015**, *14*, 301.

[7] C. H. Lee, G. H. Lee, A. M. van der Zande, W. C. Chen, Y. L. Li, M. Y. Han, X. Cui, G. Arefe, C. Nuckolls, T. F. Heinz, J. Guo, J. Hone, P. Kim, *Nat. Nanotechnol.* **2014**, *9*, 676.

[8] B. Radisavljevic, A. Radenovic, J. Brivio, V. Giacometti, A. Kis, *Nat. Nanotechnol.* **2011**, *6*, 147.

[9] X. Cui, G. H. Lee, Y. D. Kim, G. Arefe, P. Y. Huang, C. H. Lee, D. A. Chenet, X. Zhang, L. Wang, F. Ye, F. Pizzocchero, B. S. Jessen, K. Watanabe, T. Taniguchi, D. A. Muller, T. Low, P. Kim, J. Hone, *Nat. Nanotechnol.* **2015**, *10*, 534.

[10] a) X. Huang, Z. Y. Zeng, H. Zhang, *Chem. Soc. Rev.* **2013**, *42*, 1934; b) M. S. Xu, T. Liang, M. M. Shi, H. Z. Chen, *Chem. Rev.* **2013**, *113*, 3766.

[11] Q. H. Wang, K. Kalantar-Zadeh, A. Kis, J. N. Coleman, M. S. Strano, *Nat. Nanotechnol.* **2012**, *7*, 699.

[12] a) H. Fang, C. Battaglia, C. Carraro, S. Nemsak, B. Ozdol, J. S. Kang, H. A. Bechtel, S. B. Desai, F. Kronast, A. A. Unal, G. Conti, C. Conlon, G. K. Palsson, M. C. Martin, A. M. Minor, C. S. Fadley, E. Yablonovitch, R. Maboudian, A. Javey, *Proc. Natl. Acad. Sci. USA* **2014**, *111*, 6198; b) H. Jiang, *J. Phys. Chem. C* **2012**, *116*, 7664.

[13] J. Kang, S. Tongay, J. Zhou, J. B. Li, J. Q. Wu, *Appl. Phys. Lett.* **2013**, *102*, 012111.

[14] X. P. Hong, J. Kim, S. F. Shi, Y. Zhang, C. H. Jin, Y. H. Sun, S. Tongay, J. Q. Wu, Y. F. Zhang, F. Wang, *Nat. Nanotechnol.* **2014**, *9*, 682.

[15] a) R. Cheng, D. H. Li, H. L. Zhou, C. Wang, A. X. Yin, S. Jiang, Y. Liu, Y. Chen, Y. Huang, X. F. Duan, *Nano Lett.* **2014**, *14*, 5590; b) M. H. Chiu, C. D. Zhang, H. W. Shiu, C. P. Chuu, C. H. Chen, C. Y. S. Chang, C. H. Chen, M. Y. Chou, C. K. Shih, L. J. Li, *Nat. Commun.* **2015**, *6*, 7666.

[16] M. M. Furchi, A. Pospischil, F. Libisch, J. Burgdorfer, T. Mueller, *Nano Lett.* **2014**, *14*, 4785.

[17] Y. X. Deng, Z. Luo, N. J. Conrad, H. Liu, Y. J. Gong, S. Najmaei, P. M. Ajayan, J. Lou, X. F. Xu, P. D. Ye, *ACS Nano* **2014**, *8*, 8292.

[18] a) Y. J. Gong, J. H. Lin, X. L. Wang, G. Shi, S. D. Lei, Z. Lin, X. L. Zou, G. L. Ye, R. Vajtai, B. I. Yakobson, H. Terrones, M. Terrones, B. K. Tay, J. Lou, S. T. Pantelides, Z. Liu, W. Zhou, P. M. Ajayan, *Nat. Mater.* **2014**, *13*, 1135; b) X. D. Duan, C. Wang, J. C. Shaw, R. Cheng, Y. Chen, H. L. Li, X. P. Wu, Y. Tang, Q. L. Zhang, A. L. Pan, J. H. Jiang, R. Q. Yu, Y. Huang, X. F. Duan, *Nat. Nanotechnol.* **2014**, *9*, 1024; c) N. J. Huo, J. Kang, Z. M. Wei, S. S. Li, J. B. Li, S. H. Wei, *Adv. Funct. Mater.* **2014**, *24*, 7025.

[19] F. Wang, Z. X. Wang, K. Xu, F. M. Wang, Q. S. Wang, Y. Huang, L. Yin, J. He, *Nano Lett.* **2015**, *15*, 7558.

[20] a) K. A. Zhang, T. N. Zhang, G. H. Cheng, T. X. Li, S. X. Wang, W. Wei, X. H. Zhou, W. W. Yu, Y. Sun, P. Wang, D. Zhang, C. G. Zeng, X. J. Wang, W. D. Hu, H. J. Fan, G. Z. Shen, X. Chen, X. F. Duan, K. Chang, N. Dai, *ACS Nano* **2016**, *10*, 3852; b) A. Pezeshki, S. H. H. Shokouh, T. Nazari, K. Oh, S. Im, *Adv. Mater.* **2016**, *28*, 3216.

[21] S. Rathi, I. Lee, D. Lim, J. W. Wang, Y. Ochiai, N. Aoki, K. Watanabe, T. Taniguchi, G. H. Lee, Y. J. Yu, P. Kim, G. H. Kim, *Nano Lett.* **2015**, *15*, 5017.

[22] H. M. Li, D. Lee, D. S. Qu, X. C. Liu, J. J. Ryu, A. Seabaugh, W. J. Yoo, *Nat. Commun.* **2015**, *6*, 6564.

[23] C. R. Dean, A. F. Young, I. Meric, C. Lee, L. Wang, S. Sorgenfrei, K. Watanabe, T. Taniguchi, P. Kim, K. L. Shepard, J. Hone, *Nat. Nanotechnol.* **2010**, *5*, 722.

[24] Y. F. Lin, Y. Xu, S. T. Wang, S. L. Li, M. Yamamoto, A. Aparecido-Ferreira, W. W. Li, H. B. Sun, S. Nakaharai, W. B. Jian, K. Ueno, K. Tsukagoshi, *Adv. Mater.* **2014**, *26*, 3263.

[25] S. Cho, S. Kim, J. H. Kim, J. Zhao, J. Seok, D. H. Keum, J. Baik, D. H. Choe, K. J. Chang, K. Suenaga, S. W. Kim, Y. H. Lee, H. Yang, *Science* **2015**, *349*, 625.

[26] a) T. Boker, R. Severin, A. Muller, C. Janowitz, R. Manzke, D. Voss, P. Kruger, A. Mazur, J. Pollmann, *Phys. Rev. B* **2001**, *64*, 235305; b) C. Ruppert, O. B. Aslan, T. F. Heinz, *Nano Lett.* **2014**, *14*, 6231.

[27] L. Yin, X. Zhan, K. Xu, F. Wang, Z. Wang, Y. Huang, Q. Wang, C. Jiang, J. He, *Appl. Phys. Lett.* **2016**, *108*, 043503.

[28] M. Yamamoto, S. T. Wang, M. Y. Ni, Y. F. Lin, S. L. Li, S. Aikawa, W. B. Jian, K. Ueno, K. Wakabayashi, K. Tsukagoshi, *ACS Nano* **2014**, *8*, 3895.

[29] a) Y. H. Lee, X. Q. Zhang, W. J. Zhang, M. T. Chang, C. T. Lin, K. D. Chang, Y. C. Yu, J. T. W. Wang, C. S. Chang, L. J. Li, T. W. Lin, *Adv. Mater.* **2012**, *24*, 2320; b) H. Li, Q. Zhang, C. C. R. Yap, B. K. Tay, T. H. T. Edwin, A. Olivier, D. Baillargeat, *Adv. Funct. Mater.* **2012**, *22*, 1385.

[30] D. J. Perello, S. H. Chae, S. Song, Y. H. Lee, *Nat. Commun.* **2015**, *6*, 7809.

[31] a) Z. Y. Yin, H. Li, H. Li, L. Jiang, Y. M. Shi, Y. H. Sun, G. Lu, Q. Zhang, X. D. Chen, H. Zhang, *ACS Nano* **2012**, *6*, 74; b) O. Lopez-Sanchez, D. Lembke, M. Kayci, A. Radenovic, A. Kis, *Nat. Nanotechnol.* **2013**, *8*, 497.

[32] D. Cheyns, J. Poortmans, P. Heremans, C. Deibel, S. Verlaak, B. P. Rand, J. Genoe, *Phys. Rev. B* **2008**, *77*, 165332.

[33] a) H. J. Snaith, L. Schmidt-Mende, M. Gratzel, M. Chiesa, *Phys. Rev. B* **2006**, *74*, 045306; b) G. Garcia-Belmonte, J. Bisquert, *Appl. Phys. Lett.* **2010**, *96*, 113301.

[34] F. H. L. Koppens, T. Mueller, P. Avouris, A. C. Ferrari, M. S. Vitiello, M. Polini, *Nat. Nanotechnol.* **2014**, *9*, 780.

[35] C. H. Liu, Y. C. Chang, T. B. Norris, Z. H. Zhong, *Nat. Nanotechnol.* **2014**, *9*, 273.

[36] Z. X. Wang, K. Xu, Y. C. Li, X. Y. Zhan, M. Safdar, Q. S. Wang, F. M. Wang, J. He, *ACS Nano* **2014**, *8*, 4859.

[37] W. Zhang, M. H. Chiu, C. H. Chen, W. Chen, L. J. Li, A. T. S. Wee, *ACS Nano* **2014**, *8*, 8653.

[38] K. K. Manga, S. Wang, M. Jaiswal, Q. L. Bao, K. P. Loh, *Adv. Mater.* **2010**, *22*, 5265.

© 2016 WILEY-VCH Verlag GmbH & Co. KGaA, Weinheim
Adv. Funct. Mater. **2016**,
DOI: 10.1002/adfm.201601349